Hyperfine Interactions 123/124 (1999) 529–559

High-pressure studies with nuclear scattering of synchrotron radiation

Rainer Lübbers [a], Gerhard Wortmann [a] and Hermann F. Grünsteudel [b]

[a] *FB Physik, University of Paderborn, D-33095 Paderborn, Germany*
[b] *European Synchrotron Radiation Facility, F-38043 Grenoble, France*

The nuclear forward scattering (NFS) of synchrotron radiation is especially suited for probing magnetism at high pressure (h.p.), here in the Mbar range, by the nuclear resonances of ^{57}Fe and ^{151}Eu. We report on high-pressure NFS studies with the 14.4 keV transition of ^{57}Fe, presenting at first the pressure induced α–ε transformation in iron. Then a systematic study of magnetic RFe_2 Laves phases of cubic C15 structure (YFe_2, $GdFe_2$) and hexagonal C14 structure ($ScFe_2$, $TiFe_2$) at pressures up to 100 GPa (= 1 Mbar) is given. First, high-pressure NFS studies performed with the 21.5 keV resonance of ^{151}Eu are also presented, probing valence transitions in $EuNi_2Ge_2$ and the magnetism in the CsCl-type h.p. phase of EuTe. Finally, we discuss future applications, such as high-pressure studies of phonon densities of states, using the inelastic channel of nuclear scattering of synchrotron radiation.

Keywords: high pressure, magnetism, valence transition, phase transition

1. Introduction

The use of synchrotron radiation (SR) for Mössbauer spectroscopy was proposed as early as 1974 [1]. The first successful experiments were performed a decade later by the group of E. Gerdau using the 14.4 keV resonance of ^{57}Fe for nuclear Bragg-reflection (NBR) from an YIG single crystal [2]. This "exotic" resonance [3], as regarded by many members of the Mössbauer community, was not considered as being suitable for h.p. experiments, mainly because of the need for single crystals.[1] The situation changed when, in 1990, Hastings et al. [3] performed nuclear scattering experiments in the forward direction, now allowing the study of polycrystalline samples. These NFS experiments were made possible by the development of monochromators with meV resolution [4] and the use of avalanche photo diodes (APD) as fast detectors [5]. NFS experiments are in many aspects very similar to normal Mössbauer effect (ME) in transmission mode, where h.p. studies were well established from the very beginning of the spectroscopy [6]. Such h.p. experiments with NFS were now considered as very promising and were immediately performed with the advent of third generation SR sources at TRISTAN (KEK, Tsukuba) [7] and at ESRF (European

[1] High-pressure experiments could have been performed with the diffracted beam of γ-quanta in conventional energy mode [2].

Synchrotron Radiation Facility, Grenoble) [8], employing high-brilliance undulators especially designed for the Mössbauer resonances. These third-generation sources deliver SR with a 100 times higher flux and, even more importantly, with a 6 orders of magnitude higher brilliance than obtained on the bending magnets of second-generation SR sources, like HASYLAB (DESY, Hamburg), where the NBR and NFS methods were first developed. H.p. studies with the NFS method benefit both from the highly collimated SR and from the fully developed h.p. technique with diamond anvil cells (DACs). The time mode discriminates against all background radiation, which is an inherent problem of conventional ME h.p. studies. This is especially so with the ^{57}Fe-(14.4 keV)-resonance due to the 10 times more intense γ-rays of 122 and 136 keV. In the following we report on h.p. NFS studies performed at the ESRF. The article is organized as follows:

In section 2 we present the experimental set-up used for h.p. experiments at the Nuclear Resonance Beamline of ESRF and give a short introduction to the h.p. cells used in the NFS studies. We give examples of NFS spectra from magnetic and nonmagnetic samples and demonstrate the impact of texture and external polarizing fields on the NFS spectra.

Section 3 reports on the first h.p. ^{57}Fe-NFS experiments performed at the α–ε transition of iron and compares them with traditional ME experiments. We show that magnetically polarized samples allow a much easier analysis of magnetic NFS spectra and report on the impact of coherence, which gives information about the spatial distribution of α- and ε-phases in the sample.

Section 4 gives a detailed report on ^{57}Fe-NFS studies of magnetic RFe_2 Laves phases with cubic C15 structure (YFe_2 and $GdFe_2$) as well as hexagonal C14 structure ($ScFe_2$ and $TiFe_2$) at pressures up to 1 Mbar ($=100$ GPa). Due to their simple structure, these RFe_2 Laves phases are model systems for Fe magnetism in intermetallic compounds. As a function of the lattice parameter and of the substituent R, they exhibit Fe magnetism which varies from a relatively localized (high-) moment, via a more itinerant (low-) moment, to a nonmagnetic state. We also introduce the difficulties associated with the analysis of complex magnetic NFS spectra, recorded with or without a polarizing field.

In section 5 we report on the first h.p. experiments performed with the ^{151}Eu-(21.5 keV) resonance. We introduce briefly the method of measuring isomer shifts with a reference absorber and use this technique for studying a pressure induced Eu^{2+}–Eu^{3+} valence transition in an intermetallic Eu compound. Then we present h.p. NFS experiments on EuTe, a member of the widely studied Eu(II)-chalcogenides series with NaCl structure. EuTe transforms at pressures above 10 GPa into the CsCl-type phase with new magnetic properties, which are investigated here.

In section 6 we summarize the present results obtained with h.p. NFS studies and compare NFS with normal Mössbauer studies. We give an outlook on the *brilliant* future of h.p. studies with nuclear scattering of synchrotron radiation, when focusing optical elements like bent crystals, Fresnel zone plates or the compound refractive lenses are used to concentrate the SR on sample sizes as small as 10 μm. We further

discuss the use of the *inelastic channel* of nuclear scattering to perform studies of phonon density of states under high pressure.

2. Experimental techniques

2.1. Experimental set-up for h.p. NFS studies

A typical set-up for the ^{57}Fe-resonance is shown in figure 1. The radiation from an undulator, tuned with its first harmonic to 14.4 keV is monochromatized by a high-heat-load Si(1, 1, 1) double crystal monochromator (PM) to a bandwidth of 2.5 eV and then further narrowed down to about 6 meV by a "nested" high-resolution monochromator (HRM). This beam was used to excite the 14.413 keV levels of the ^{57}Fe nuclei in the absorber, here shown schematically within a diamond-anvil cell. The detector (D) measures the forward scattered intensity of SR as a function of time after excitation. These γ-quanta are emitted strictly in the forward direction for elastic (i.e., without recoil) absorption and emission processes and are delayed in time due to the relatively long nuclear lifetime (141 ns). The time-mode detection of the NFS spectra allows an easy discrimination against all other electronically scattered radiation, which occurs almost instantaneously within the width of the SR bunches (100 ps). The 6 GeV storage ring of ESRF was operated for the NFS experiments in 16-bunch mode providing a time window of 176 ns between the bunches, which is essential for the detection of beat modulations in the time response of delayed nuclear counts.

2.2. Basic properties of NFS spectra; effects of texture and magnetic polarization

Figure 2 presents NFS spectra of non-magnetic stainless steel and magnetic iron, the latter measured without and with an external polarizing field of 0.6 T. For comparison, the corresponding conventional Mössbauer spectra are shown in the right-hand panel of figure 2. The time spectrum of the nonmagnetic sample shows only the exponential decay, modified in addition by thickness effects, resulting in a speed-up of

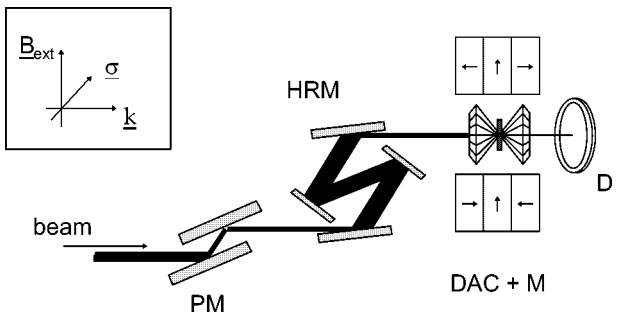

Figure 1. Experimental set-up at the Nuclear Resonance Beamline ID18 (ESRF) with schematic diamond-anvil cell (DAC), external magnets (M), premonochromator (PM), high-resolution monochromator (HRM) and avalanche photo diode as detector (D).

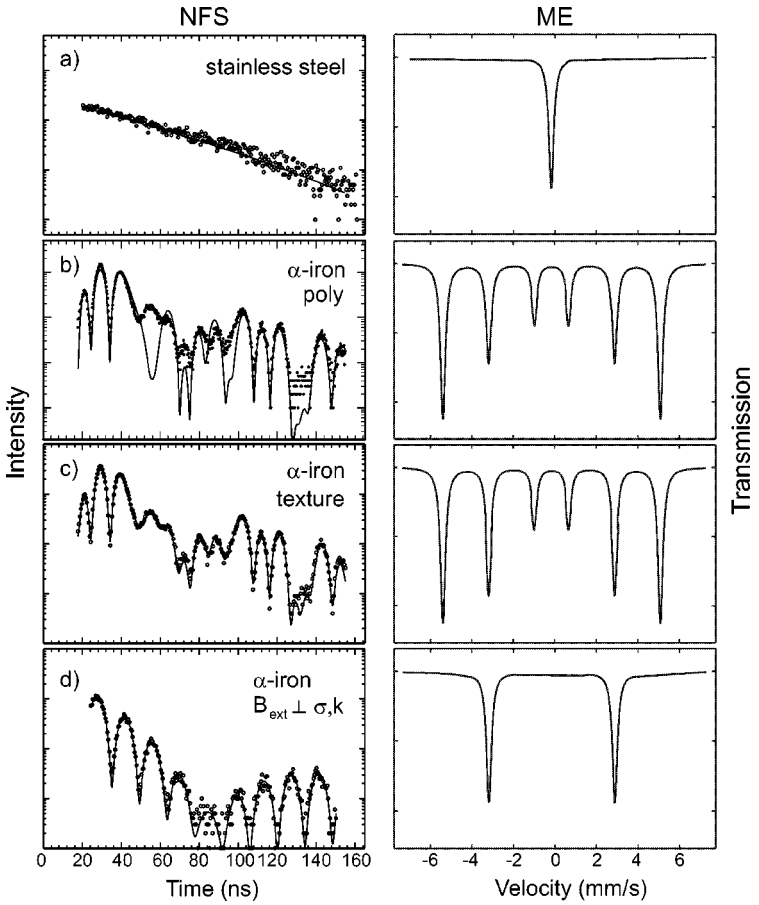

Figure 2. Left-hand panel: NFS spectra of nonmagnetic stainless steel (a) and magnetic iron (b)–(d). The iron spectrum measured without external field is shown together with a fit assuming a random orientation of the magnetic hyperfine axis (b) and a magnetic texture (20%) within the sample plane (c). Part (d) shows the time spectrum for a totally polarized iron foil in an external field perpendicular to the σ-polarization and the direction of the incoming beam. Right-hand panel: Corresponding spectra (schematic) from conventional Mössbauer effect (ME).

the collective nuclear decay. For magnetic iron, all six possible transitions between the $3/2$ excited and $1/2$ ground state are excited by the broadband (meV) SR pulse. The decay shows a complex intensity modulation, arising from the superposition of the transition frequencies. This NFS spectrum is certainly more difficult to analyse than the traditional six-line ME spectrum due to the fact that the shape of a NFS time response is strongly influenced by thickness effects, thickness distributions and/or texture effects (magnetic and/or crystallographic) in the absorber.

Since we used polycrystalline powder samples with thickness distributions in most of our h.p. NFS studies and since texture effects are inevitable in an h.p. cell, we show, as the simplest case, the impact of a magnetic texture on the NFS spectrum of

an ^{57}Fe foil (thickness 3 μm), as used for calibration purposes in ME studies. Figure 2 shows the NFS spectrum of this foil assuming (b) no texture and (c) a magnetic texture for the fit (done with CONUSS [9]). It is evident that the fit without texture is only a poor representation of the data, whereas the fit including texture delivers a much better adjustment. In a normal magnetic ME spectrum, the texture can be considered by one additional parameter, describing the deviation of the averaged magnetization in the absorber plane from the average (magic) angle 54.7°. In the case of a magnetic (thin) iron foil, the magnetization normally lies predominantly in the plane of the foil, which results in an averaged polarization angle larger than 54.7°. In the fit of the NFS spectra, the adjustment of the magnetic texture needs two parameters due to the polarization of the SR, one describing the texture within the foil and the other with respect to the $\vec{E}$ vector of the SR.

The polarization of the SR is fully exploited in the spectrum of a magnetically aligned absorber shown in figure 2(d). Here the axis of magnetization is perpendicular to both the $\vec{E}$ and $\vec{k}$ vector of the SR (see figure 1), resulting in a much simpler NFS spectrum than that of a non-aligned Fe foil. Only the two $\Delta m = 0$ transitions of the ^{57}Fe resonance contribute to the NFS spectrum so that the corresponding beat frequency is much easier to analyse. The magnetic hyperfine field can be determined with high accuracy from the symmetric and periodic sequence of beats, modified only by thickness effects, resulting in the present case in a Bessel minimum at 85 ns.

One should mention that such simplified magnetic spectra are difficult to obtain in a conventional ME experiment, where the source is normally not polarized. The spectrum in figure 2(d) resembles an ^{57}Fe quadrupole spectrum, where the excited $3/2$ state is split, but not the ground state. Since in the case of the magnetically polarized absorber the two $\Delta m = 0$ transitions belong to different ground and excited states (different nuclei), the beating in the NFS spectrum demonstrates the spatial coherence of the NFS process within the coherence volume of the SR. We refer to [3,10] for a detailed description of these phenomena which can yield (via the transverse coherence length) information about the spatial distribution of different phases in the sample (see also section 3.3).

2.3. High-pressure techniques with diamond-anvil cells

Diamond-anvil cells have been used successfully in normal ME for almost two decades [11]. We refer to [12] for an outstanding application at pressures above 1 Mbar and to [13,14] for review articles. For the present studies we developed diamond-anvil cells (DAC) made from a nonmagnetic CuBe alloy (figure 3). This allows the application of external magnetic fields to the pressurized samples to exploit the above-mentioned polarization properties of the SR. The large openings in the cell perpendicular to the direction of the SR beam are used to bring the pole shoes of an array of Nd–Fe–B permanent magnets as near as possible to the sample. With this simple array, homogeneous fields up to 0.8 T can be obtained. The cells were also

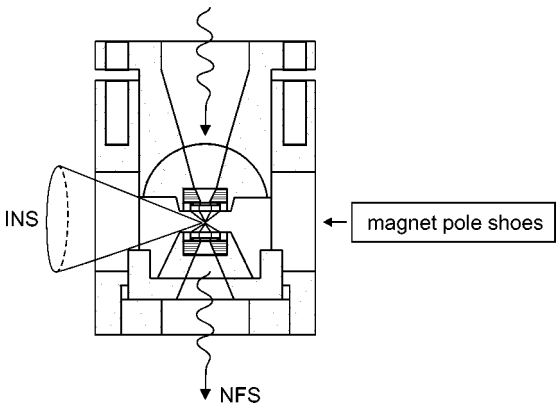

Figure 3. Sketch of the diamond-anvil cell (DAC) with large openings perpendicular to the beam, used for the pole shoes of the permanent magnet or for the detection of inelastically scattered radiation (INS).

used in normal ME studies using point sources and special collimators to minimize the background radiation as described in [14].

The transmission through the diamond anvils (5 mm) is about 20% for ^{57}Fe (14.4 keV) and 50% for ^{151}Eu (21.5 keV). Depending on the envisaged pressure range, the sample diameter within the $Ta_{90}W_{10}$ gasket varied from 250 μm (50 GPa) to 80 μm (100 GPa). A 4 : 1 mixture of methanol/ethanol served as the pressure transmitting medium. The pressure was monitored before and after each measurement using the ruby fluorescence method [15]. In addition, XRD measurements were performed on the pressurized samples before and after some of the NFS studies, yielding directly the lattice parameters. Most of the present h.p. studies were performed at room temperature. Future studies at low or high temperatures have to cope with the problem that the pressure in the cell may change with temperature. For such measurements, an in-situ pressure determination in the cryostat or oven is inevitable. The Paderborn group has already developed such a technique for h.p. XAS studies conducted at low temperature [16].

Finally, the above DAC was designed to allow studies of phonon densities-of-states under h.p. using the inelastic channel of the nuclear scattering of SR. In such experiments [17,18], one observes the reemission of γ- or X-ray fluorescence rays in the 4π direction originating from inelastic absorption processes. In this case, the large openings of the cell allow two APD detectors to be placed near the pressurized sample.

3. The α/ε-phase transition in metallic iron as an example for h.p. NFS studies

3.1. First h.p. ^{57}Fe-NFS experiments at the Troika Beamline of ESRF

Metallic iron undergoes a pressure-driven phase transformation from magnetic α-iron to nonmagnetic ε-iron at room temperature, which was first reported by Bancroft et al. [19]. The transition occurs above a pressure of 13 GPa. It was studied in the

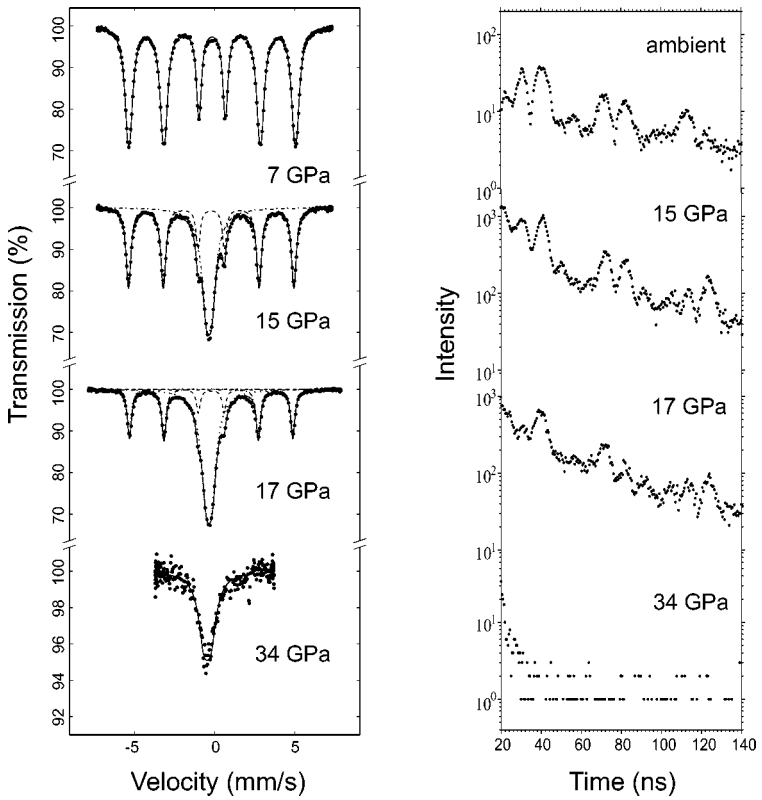

Figure 4. ^{57}Fe-NFS spectra for the $\alpha \rightarrow \varepsilon$ transition in iron (right-hand panel), measured at the Troika Beamline without external field. The corresponding Mössbauer spectra are shown in the left-hand panel.

early days of the Mössbauer effect and is directly evidenced in ME spectra by the appearance of an additional unsplit line near the centre of the six-line spectrum of magnetic α-Fe [20–22] (see also figure 4). With increasing pressure, this unsplit line grows continuously until at pressures above 20 GPa only the ε-phase remains.

The α/ε-phase transition in iron, monitored by ME and other methods, is well documented in the literature. However, different pressure values exist for both the onset and the completion of the transition. These discrepancies can be explained by the dependence of the transition pressure on the shear strength of different pressure transmitting media employed in these studies [22,23].

The first NFS experiments at the $\alpha \rightarrow \varepsilon$ phase transition of iron, accompanied by normal ME studies, were performed at the Troika Beamline (ID 10A) at ESRF in 1994. A set-up similar to that shown in figure 1 was installed for these first NFS studies at ESRF [8]. In a first run a 2.5 μm thin iron foil, enriched to 95% in ^{57}Fe, was pressurized in a diamond-anvil cell (with 1.0 mm anvil flat and 0.5 mm sample diameter) up to 17 GPa. For an additional spectrum at 34 GPa, now in the pure ε-phase, diamonds with 0.7 mm anvil flat diameter and a sample diameter of 100 μm were used.

Figure 4 exhibits the NFS spectra of the $\alpha \rightarrow \varepsilon$ transition of iron and, for comparison, the corresponding ME spectra, measured before or after the NFS experiments in the same h.p. cell. Details are reported in [24,25]. The nonmagnetic ε-phase (unsplit line) occurs in coexistence with the magnetic α-phase at 15 and 17 GPa and as a pure phase at 34 GPa. The parameters derived for the α- and ε-phase from the ME spectra are in good agreement with the literature [19–22].

The NFS spectra of the $\alpha \rightarrow \varepsilon$ transition, shown in the right-hand panel of figure 4, do not have the statistical accuracy of most of the h.p. NFS spectra shown later in this review. This was due to the limited beamtime available for these preliminary experiments at the Troika Beamline, where the output of resonant γ-quanta was much lower than obtained later at the Nuclear Resonance Beamline. Exploratory in character, these spectra demonstrated already convincingly the feasibility of the NFS method for h.p. studies. The spectrum of α-Fe at ambient pressure closely resembles that shown in figure 2(b). The influence of the ε-phase on the time spectra at 15 and 17 GPa is evidenced through the faster decay and a modulation of the beat structures. The effective absorber thickness (per resonance line) in the pure ε-phase is about four times larger than that of the α-phase, which is documented in the steep decay of the 34 GPa spectrum, yielding almost no NFS quanta after 40 ns. Due to the smaller absorber diameter, the count rate was only 1 s^{-1} and 10 times smaller than that of the other h.p. spectra. Consequently the statistics were not good enough to observe the Bessel beat minimum expected around 50 ns for this effective thickness. The analysis of the NFS spectra is documented in [24,25]. It proved difficult, especially in the coexistence region of the α- and ε-phase, due to reasons described in the next sections.

3.2. ^{57}Fe-NFS studies of the $\alpha \rightarrow \varepsilon$ transformation in Fe in an external field

A second series of NFS measurements on the $\alpha \rightarrow \varepsilon$ transformation of iron was performed in 1996 at the newly installed Nuclear Resonance Beamline ID18 of ESRF. In order to simplify the NFS spectra as discussed in section 2.2, an external field of about 0.6 T was applied to the absorber in the h.p. cell.

Figure 5 (top) shows the NFS spectrum of iron in the pure α-phase at a modest pressure of 3 GPa. The data reveal the expected time response for α-Fe. The regular beat pattern shows a single frequency, from which a hyperfine field of 32.4 T can be extracted (corresponding to 33.0–0.6 T for the polarizing field). Thickness effects are less pronounced than in the corresponding spectrum shown in figure 2(d). NFS spectra within the pressure range of the $\alpha \rightarrow \varepsilon$ transformation are also shown in figure 5. At 14 GPa, the influence of the ε-phase is already quite pronounced and opposed to the pure α-Fe spectrum, the minima of the beats are no longer equally spaced, indicating that at least part of the spectrum originates from a coherent addition of the scattering from α- and ε-domains. With a further increase in pressure the influence of the nonmagnetic ε-phase becomes dominant. At 21 GPa the sample is almost completely transformed into pure ε-Fe and the NFS spectrum is modified only by a single Bessel minimum at 50 ns. This originates from the increased thickness in comparison to that

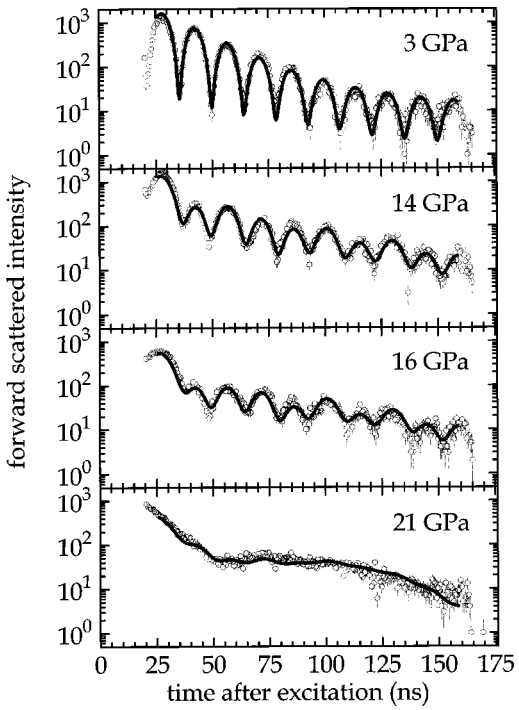

Figure 5. ^{57}Fe-NFS spectra for the $\alpha \rightarrow \varepsilon$ transition in iron, measured in an external field of 0.6 T.

of the magnetically split absorber. The fitting of the NFS spectra is described in the next section.

3.3. The impact of coherence on the NFS spectra of mixed α-Fe and ε-Fe phases

Both the α- and ε-phases of Fe coexist in the rather broad transition region. The question therefore arises what kind of spatial distribution is present in the pressurized absorber. For this purpose different kinds of simulated superpositions are shown in figure 6 for α- and ε-domains in an intensity ratio 1 : 1. Figure 6(a) indicates the energy spectrum for a relatively thick absorber. Figure 6(b) shows the corresponding time response for a coherent addition of both phases. The forward scattered amplitude includes a sum over three resonance levels, here $a(\alpha) + b(\alpha) + c(\varepsilon)$. The resulting forward scattered intensity, proportional to $(a + b + c)^2$, is shown in figure 6(b). A new dominant beat structure occurs with a period of about 30 ns, corresponding to the energy difference of $\pm 30\Gamma_0$ between the unsplit line of the ε-phase and the magnetically split lines of the α-phase, in addition to the $60\Gamma_0$ magnetic splitting of the pure α-phase. An incoherent addition of the two phases is shown in figure 6(c), which basically corresponds to a time response of the scattered intensity proportional to $(a + b)^2 + c^2$. The beat frequency corresponds to the magnetic splitting of the $\Delta m = 0$ transitions in the α-phase, the modulation of the beat amplitudes arises from the Bessel minimum of the ε-phase at 75 ns.

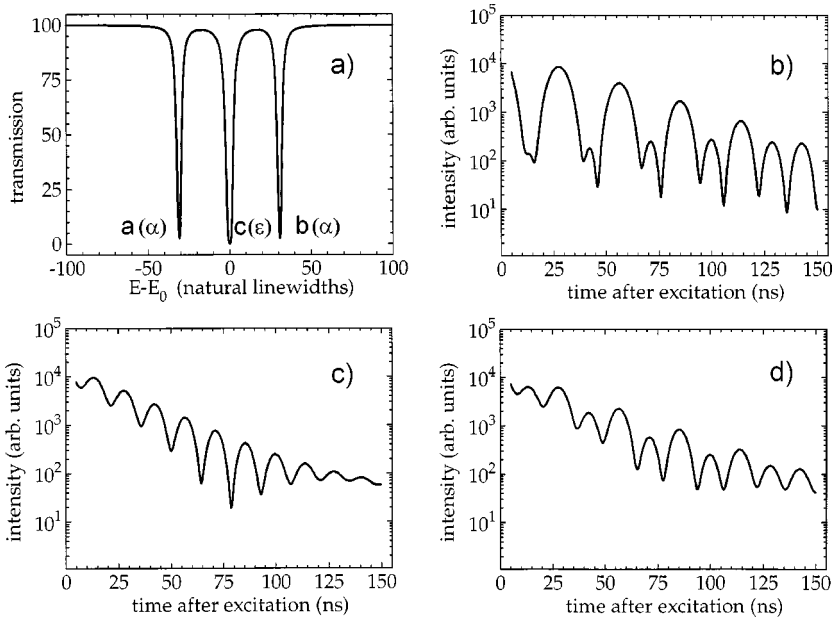

Figure 6. (a) Simulated NFS spectra for different superpositions of resonance lines $a(\alpha)$, $b(\alpha)$ and $c(\varepsilon)$, denoted in the energy spectrum. Part (b) shows the coherent sum of all three lines, and part (c) the incoherent addition of the two iron phases, i.e., a/b and c. Part (d) presents a mixture of (b) and (c). For details see text.

Since the NFS spectra measured in the α/ε phase coexistence range, shown in figure 5, correspond neither to figure 6(b) nor to figure 6(c), but more to their average, figure 6(d) presents a mixture of the two cases with the following assumptions: the scattering intensity arises from incoherent contributions of 33% pure α-phase, 33% pure ε-phase and 33% from "well mixed" α/ε-regions of the sample where half of the nuclei are in the α-phase or in the ε-phase. This simulated spectrum closely resembles that of the measured NFS spectrum at 14 GPa. Therefore all spectra in the coexistence range of α- and ε-phase were analysed as the incoherent sum of these three contributions, now with variable relative weights, denoted w_α, w_ε and $w_{\alpha/\varepsilon}$. The results of the fit are shown in figure 7.

For calculating the NFS-spectra of the α-phase and the α/ε-phase, the well-known pressure dependence of isomer shifts [21] and the hyperfine field [22] has been taken into account. The small difference in isomer shift between the α- and ε-phase of $-0.14\ \mathrm{mm\,s^{-1}}$ (see ME spectra in figure 4 and [21]) leads to an additional (small) modulation of the transition frequencies between α- and ε-phase, which was included in the fits. Contributions of a possible quadrupole splitting in hexagonal ε-Fe (with an upper limit of $0.1\ \mathrm{mm\,s^{-1}}$ [22]) were tested but found to be negligible in the present time window of the NFS spectra.

The plot of the relative weights of different contributions in figure 7 reflects the α/ε-phase transition in iron. The width of the transition compares well with that

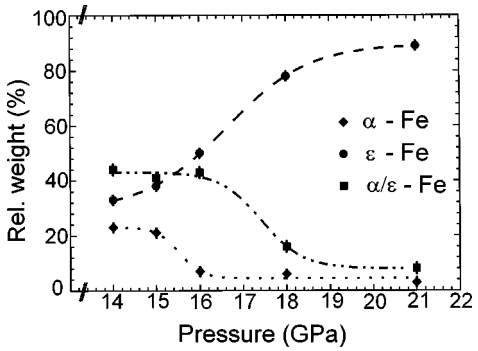

Figure 7. Relative weight for different contributions from α-, ε- and mixed α/ε-phase in the NFS spectra. The values at 15 GPa are derived from the measurements of the nonmagnetized absorber (figure 4).

observed in [22,23] for the methanol/ethanol mixture used as pressure transmitting medium. The relative intensity of the different phases, especially of the mixed α/ε-phase, contains information about the spatial distribution of the phases. For a further discussion, we need information about the transverse coherence length in the present experimental set-up. Following the argumentation of [10, eq. (6)], an effective transverse coherence length $L_{\rm tr}$ can be calculated for the experimental set-up according to

$$L_{\rm tr} \approx \frac{\lambda}{2\pi\sigma_{\rm D}/D}. \tag{3.1}$$

λ is the wavelength of the radiation, here 0.86 Å, D is the detector-to-sample distance, here $\approx$1 m, and $\sigma_{\rm D}$ is the detector acceptance. Due to the small detector-to-sample distance, all other terms in eq. (6) of [10] become negligible. Taking the beam size as given by the diameter of the gasket hole (0.2 mm) as detector acceptance $\sigma_{\rm D}$, we derive an effective transverse coherence length $L_{\rm tr} \approx 160$ Å for this experimental arrangement. Within this length perpendicular to the propagation direction of the beam, the scattering amplitudes of different phases in the sample add coherently. Of course, all different phases lying in the longitudinal path of the X-rays through the sample add coherently.

The α–ε transition is known to be martensitic [23]. In such a transformation small regions of the new (ε-) phase are formed in the precursor (α-) phase, increasing in size and number with increasing pressure. From figure 7 one can see that the coherent α/ε contribution is rather large at 14 GPa (where the transition is about half completed). Thus one can conclude that α- and ε-regions lie "behind each other" from the perspective of the beam. Since the pressurized sample is 2 μm thick (and 200 μm in diameter), the different domains must be well below 1 μm in size to add to the coherent α/ε response. When, on the other hand, the size of ε-phase domains is comparable to the sample thickness, the coherent α/ε response should be rather weak. This is the case when the transition is almost completed.

Finally, we want to point out that a simple separation of the two phases in the pressurized absorber due to an unavoidable pressure gradient can be unambiguously discarded as a reason for the shape of the measured NFS intensities. In such a scenario,

the ε-phase would grow out homogeneously from the centre of the sample to the outside with increasing pressure, yielding an incoherent addition of α- and ε-phase as shown in the simulated NFS spectrum in figure 6(c). It should be emphasized that this kind of information on the spatial distribution of different phases cannot be obtained from energy resolved ME studies, where all recorded resonance effects are incoherent.

4. ^{57}Fe-NFS studies of RFe_2 Laves phases

4.1. Structures and magnetic properties of RFe_2 Laves phases; NFS spectra at ambient pressure; effect of external fields

We turn now to h.p. NFS studies of magnetic RFe_2 Laves phases with either cubic C15 or hexagonal C14 structure. These structures are shown in figure 8. The cubic C15-phase is a very common structure for RM_2 intermetallics with R as larger metal ion like trivalent Y and Ln (lanthanide) metals and M = 3d metals like Mn, Fe, Co, Ni, and also simple metals like Al. Depending on the ratio of the ionic radii of R and M as well as on the averaged conduction electron number the C15 or C14 structure appears [26]. The hexagonal C14 phase is also quite common, for instance with R as a trivalent, tetravalent or pentavalent d-metal like Sc, Ti, Hf, Ta. Here we concentrate on RFe_2 systems to study the magnetic properties of the itinerant Fe 3d-moments and their interplay with Ln 4f-moments, like Gd with the large $S = J = 7/2$ spin-only 4f-moment.

In the C15 structure, the R sites build up a diamond lattice, whereas the M atoms form tetrahedrons connected via their corners to fill up the empty interstices. In the C14 structure, the R sites form a hexagonal lattice, resembling in some aspects a hcp lattice. The interstices are filled again by M tetrahedrons, now sharing common planes and corners. In both C15 and C14 structures the R and M sites are similarly coordinated, the M sites have 6 M and 6 R nearest neighbours. This joint coordination

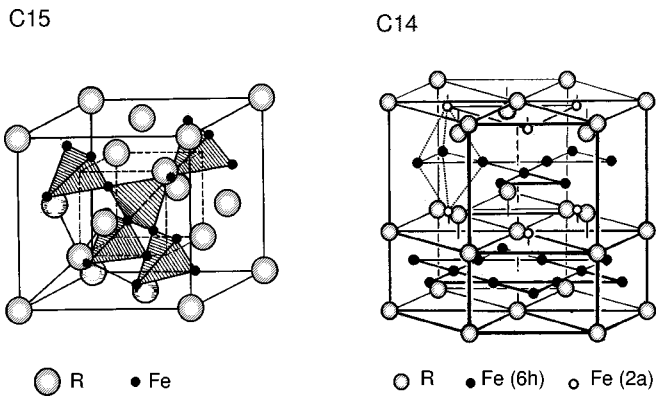

Figure 8. C15 and C14 structures of RFe_2 Laves phases.

number of 12 makes the C15 and C14 structure similar to the fcc and hcp lattice of monoatomic metals, here to γ-Fe and ε-Fe, the fcc and hcp allotropes of iron.

In RFe_2 systems with C15 structure, all R and Fe sites are crystallographically equivalent. The R sites have local cubic symmetry, whereas the Fe sites have local C_3 symmetry, which results, in terms of hyperfine interactions, in an axially symmetric electric field gradient (EFG) along the $[1, 1, 1]$ directions. When magnetically ordered, the local magnetic behaviour of the Fe sites depends sensitively on the direction of magnetization. The simplest case is when the magnetization is along the crystallographic $[1, 0, 0]$ direction, as in the case of R ions like Dy and Er with large 4f orbital moments. Then all Fe sites remain magnetically equivalent and the magnetic hyperfine field and the EFG at the Fe sites form the "magic" angle $\beta = 54.7^\circ$. When the magnetization is along the $[1, 1, 1]$ direction, which is the case in RFe_2 C15-phases with nonmagnetic R metals like Y and Lu [26], then there are two magnetically nonequivalent Fe sites in the ratio 3 : 1; the majority site with an angle $\beta_1 = 70.5^\circ$, the minority site with $\beta_2 = 0^\circ$. In the case of $GdFe_2$ with the large $S = 7/2$ moment, there is a more complex, basically ferrimagnetic (antiparallel) interaction between the two spin systems. The canted spin structure of the Fe sublattice is approached by at least three sublattices with angles β varying between 40° and 75° [27]. As shown in many ^{57}Fe-ME studies (for a collection see [26]), there is in all RFe_2 C15-phases a clear correspondence between the angle β and the magnitude of the hyperfine field, reflecting the transfer mechanism of hyperfine fields and their dependence on the direction of magnetization.

The RFe_2 C14-phases exhibit magnetic properties related to the hexagonal structure. The two Fe sites, 6h and 2a, are crystallographically and magnetically different. $ScFe_2$ is ferromagnetically ordered with the Fe moments of both 6h and 2a sites directed along the c-axis. $TiFe_2$, on the other hand, shows an interesting antiferromagnetic structure: the 6h sites are ferromagnetically ordered within the planes with the moments oriented along the c-axis, the 6h planes, however, couple antiferromagnetically, leaving the 2a sites in a nonmagnetic position. In the $Sc_{1-x}Ti_xFe_2$ alloy series, this transition from ferro- to antiferromagnetism can be reached at $x = 0.65$ [28]. Since the substitution of Sc by Ti is accompanied, besides a change in the averaged conduction electron number, by a decrease of the lattice parameters, we expected that this magnetic transition can also be induced in pure $ScFe_2$ by the application of pressure.

Before presenting h.p. data, we show in figure 9 the NFS spectra of C15-phase YFe_2 and C14-phase $ScFe_2$, measured at ambient pressure at the BW4 Beamline of HASYLAB in 2-bunch mode, providing a time window of 480 ns. YFe_2 and $ScFe_2$ represent the case for pure iron magnetism with Curie temperatures of $T_C = 535$ K and 540 K, respectively [26]. The spectra were measured at 300 K without external field and at 77 K with a polarizing field of 3 T, provided by a superconducting solenoid.

The NFS spectrum of YFe_2 without a polarizing field was fitted, as described above, with two sites in the ratio 3 : 1 with $B_{hf,1} = 18.6$ T and $B_{hf,2} = 17.8$ T, a quadrupole splitting $\Delta E_Q = eQV_{zz}/2 = (-)0.24$ mm s^{-1} and $\beta_1 = 70.5^\circ$ and $\beta_2 = 0^\circ$ [26]. Similar to the case of α-Fe without polarization, a small magnetic

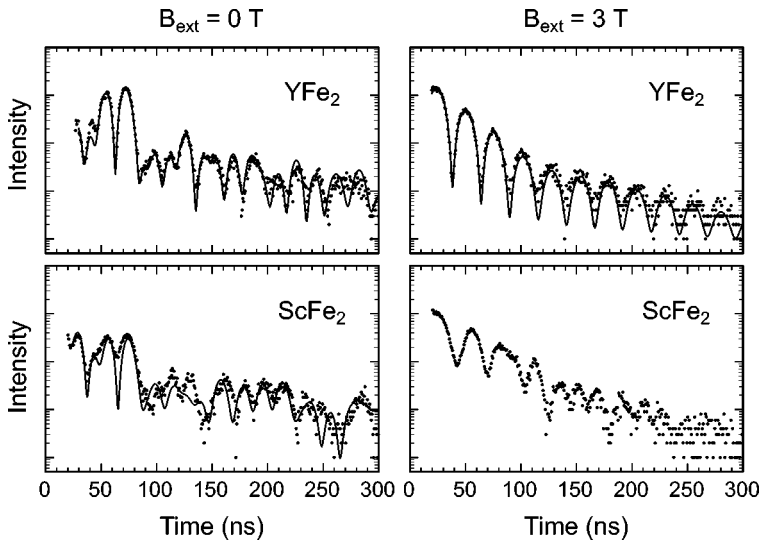

Figure 9. ^{57}Fe-NFS spectra of YFe_2 and $ScFe_2$, measured at BW4 (HASYLAB) without (300 K, left-hand panel) and with (77 K, right-hand panel) external field of 3 T.

texture has to be taken into account. This texture is actually not expected for a powdered sample of a cubic compound embedded in paraffin, but may be due to remaining magnetization from previous experiments in external fields.

With the application of an external field $B_{\text{ext}} = 3$ T at 77 K, the magnetization in the polycrystalline YFe_2 sample is fully aligned in the same configuration as in the case of α-Fe in figure 2(d). The same "simple" periodic beat structure appeared, now with a modulation frequency corresponding to the smaller splitting of the $\Delta m = 0$ transitions in YFe_2. The polarized NFS spectrum was adjusted with one magnetic field, B_{eff}, and a random orientation of the quadrupole interaction with respect to B_{eff}, by calculating and adding 48 subspectra in the CONUSS program package with varying angles β from 0° to 90°. The fitted value of $B_{\text{eff}} = (-)18.0$ T leads to $B_{\text{hf}} = B_{\text{eff}} - B_{\text{ext}} = -21.0$ T at 77 K (the negative sign of B_{hf} in all RFe_2 Laves phases is well established [26]). The random quadrupole interaction is reflected by a damping of the magnetic beat structure (the quadrupole splitting of 0.24 mm s^{-1} is small in comparison to the magnetic splitting, here 4 mm s^{-1}).

The corresponding NFS spectra of $ScFe_2$, shown in figure 9 (right-hand panel), are not fitted as well as those of YFe_2 for two reasons: First, this sample, enriched with 30% ^{57}Fe, was relatively thick with a large thickness distribution and showed also magnetic texture effects. Second, $ScFe_2$ is, due to its hexagonal structure, magnetically "hard" and needs an external field of 4.5 T for a full alignment [26]. The NFS spectrum in the applied field of 3 T already shows a strong modification, but not the equally spaced beat structure as observed for YFe_2 in this external field. Adjustment of both $ScFe_2$ spectra with the CONUSS program reveals, however, values of the hyperfine fields, $B_{\text{hf},1} = B_{\text{hf},2} = -17.8$ T, in very good agreement with B_{hf} values derived from

normal ^{57}Fe-ME studies [26,29]. The quadrupole interaction in $ScFe_2$ is different for the two sites: the 2a site has an axially symmetric EFG parallel to the c-axis (the axis of magnetization), the 6h site experiences an EFG tensor with the main axis perpendicular to the c-axis and a large asymmetry parameter η. This behaviour of the quadrupole splitting with $\Delta E_Q = (-)0.40$ mm s^{-1} for both sites is very similar to the case of $TiFe_2$ [29,30].

4.2. H.p. NFS spectra with and without a polarizing field: YFe_2 and $GdFe_2$

Now we present h.p. NFS spectra of YFe_2 together with those of $GdFe_2$ to compare the case of pure iron magnetism in YFe_2 with that of $GdFe_2$, where the magnetic Gd sublattice strongly influences the magnetic properties, as evidenced by the larger (averaged) Fe hyperfine field at 300 K, $B_{hf} = 21.5$ T ($YFe_2 = 18.3$ T) and the ferrimagnetic ordering temperature, $T_C = 790$ K (YFe_2: $T_C = 535$ K). The h.p. experiments were performed at 300 K with a polarizing field of 0.75 T, supplied by a permanent magnet array to the centre of the h.p. cell (see figures 1 and 3). Figure 10 (left panel) shows typical NFS spectra of YFe_2 at various pressures with the polarizing field in the same configuration as explained above. The simple beat pattern at ambient pressure, now measured at 300 K with $B_{ext} = 0.75$ T, is similar to that measured at 77 K with $B_{ext} = 3.0$ T. The fit reveals a hyperfine field of 18.6 T and a quadrupole splitting of $(-)0.24$ mm s^{-1}. With increasing pressure we observe a decrease of the magnetic hyperfine fields and an increase of the quadrupole splitting, resulting in an increased damping of the magnetic beat structures. This is best demonstrated by the spectrum at 50 GPa, where the simple magnetic beat pattern is already strongly modified. Going further up with pressure, there is a drastic change in the spectrum at 71 GPa, now being dominated by a quadrupole interaction with a period of 110 ns (corresponding to $(-)0.8$ mm s^{-1} splitting), slightly modified by a magnetic site with a hyperfine field of 9 T. The spectrum at 105 GPa arises solely from a quadrupole interaction with a beat period of 100 ns (corresponding to $(-)0.85$ mm s^{-1} splitting). Additional studies of this sample at 105 GPa in a closed-cycle He cryostat revealed the complete absence of magnetic interactions down to temperatures as low as 15 K. From this behaviour and additional NFS and ME spectra measured without an external field, we can state that the magnetic ordering temperature in YFe_2 is suppressed from 535 K at ambient pressure to 300 K around 75 GPa and to below 15 K at 105 GPa.

A similar series of NFS spectra were taken from $GdFe_2$ at 300 K up to 105 GPa. The variation of the (averaged) hyperfine fields, shown in figure 12, demonstrates that $GdFe_2$ remains magnetically ordered well above 300 K in the whole pressure range. This different behaviour, compared to YFe_2, is clearly caused by the magnetic Gd sublattice, since the structural properties and compressibilities of YFe_2 and $GdFe_2$ are very similar. For both samples the lattice parameters were determined by energy-dispersive XRD studies at HASYLAB up to 105 GPa [31]. We know from additional Mössbauer and resistivity studies [32] that the Gd sublattice orders around 120 K at ambient pressure and that this ordering temperature increases with pressure. From

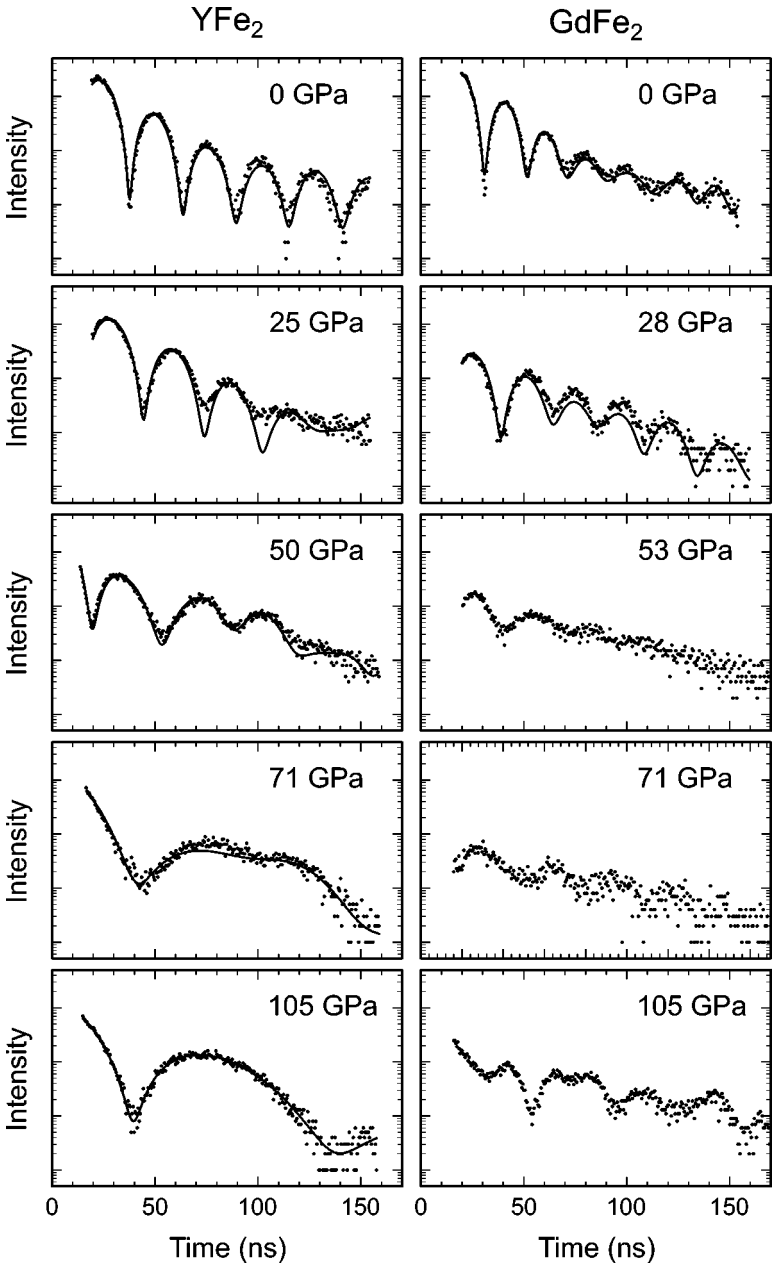

Figure 10. ^{57}Fe-NFS spectra of YFe_2 and $GdFe_2$ at various pressures, measured in an external field of 0.75 T.

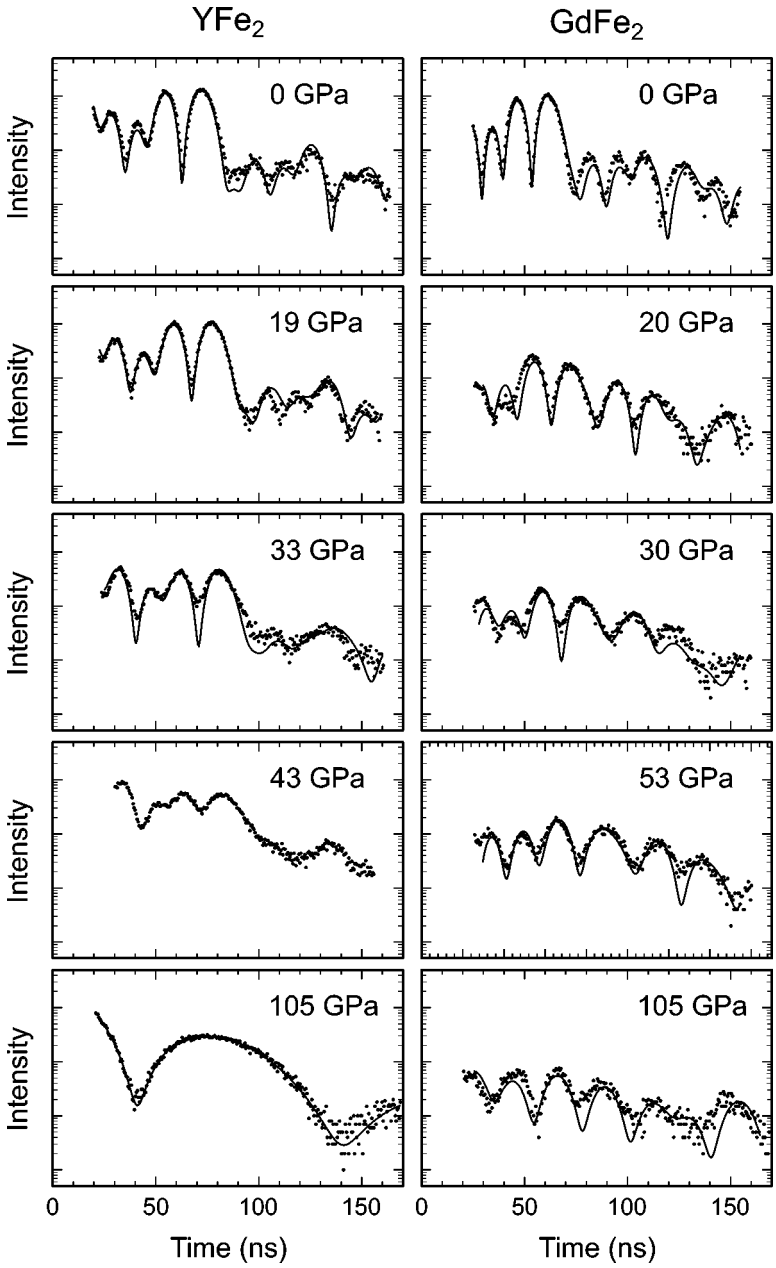

Figure 11. Fe-NFS spectra of YFe_2 and $GdFe_2$ at various pressures, measured without external field.

figures 10–12 one may deduce that the magnetic strength of the Gd sublattice surpasses that of the Fe sublattice somewhere above 50 GPa, thereby taking over the leading role in the Fe moment formation by the 4f–5d–3d interaction between the localized Gd 4f moment and the itinerant Fe moment. The different magnetic behaviour of Fe

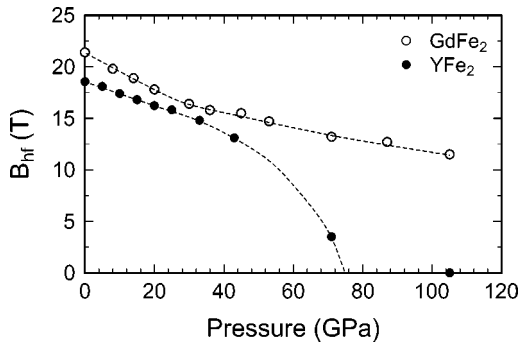

Figure 12. Average hyperfine fields for YFe_2 and $GdFe_2$.

in YFe_2 and $GdFe_2$ is, to our opinion, of importance for the basic understanding of the formation and stability of Fe moments in rare-earth intermetallics, such as hard magnets like $Nd_2Fe_{14}B$.

4.3. H.p. NFS spectra of $ScFe_2$, and comparison with $TiFe_2$ and $Sc_{0.4}Ti_{0.6}Fe_2$

In $ScFe_2$, we observe from a series of h.p. NFS spectra, taken at 300 K, a strong decrease of the magnetic hyperfine fields with pressure (see figure 13). Above 26 GPa, the beat structure of the NFS spectrum changes drastically. The spectrum at 35 GPa is similar to that of antiferromagnetic $TiFe_2$ at 200 K and ambient pressure (not shown here). Additional conventional ME studies reveal a situation similar to a previous h.p. ME study of $TiFe_2$ [30], namely magnetic 6h sites with $B_{\mathrm{hf},1} = 12$ T and a nonmagnetic 2a site. The 51 GPa NFS spectrum of $ScFe_2$ at 300 K indicates the absence of magnetic order (the minimum is caused by thickness effects). At lower temperatures the NFS spectra of $ScFe_2$ at 51 GPa exhibit a small magnetic hyperfine field ($B_{\mathrm{hf},1} = 4$ T at 50 K). From the temperature dependence of $B_{\mathrm{hf},1}$, observed from NFS and ME spectra, we derive $T_N = 300(10)$ K [30].

The pressure-induced change from a ferromagnetic (fm) to an antiferromagnetic (afm) state in $ScFe_2$ corresponds to the magnetic behaviour observed in the $Sc_{1-x}Ti_xFe_2$ series as a function of Ti concentration [28]. This fm–afm transition resembles that observed in γ-Fe layers stabilized on Cu(Au) substrates with varying lattice parameters [33].

4.4. Magnetic phase diagram of RFe_2 systems; Wohlfahrt model of band magnetism

In this section we discuss the pressure-induced changes of the magnetic ordering behaviour and Fe moment formation observed in the investigated Laves phases. In figure 14(a) we present a plot of the magnetic ordering temperatures in C15 and C14 RFe_2 compounds as a function of the Fe–Fe distance together with the pressure-induced changes as derived from the present studies and, indicated by arrows, from earlier resistivity studies up to 3.5 GPa [34]. At the top of figure 14(a), we indicate

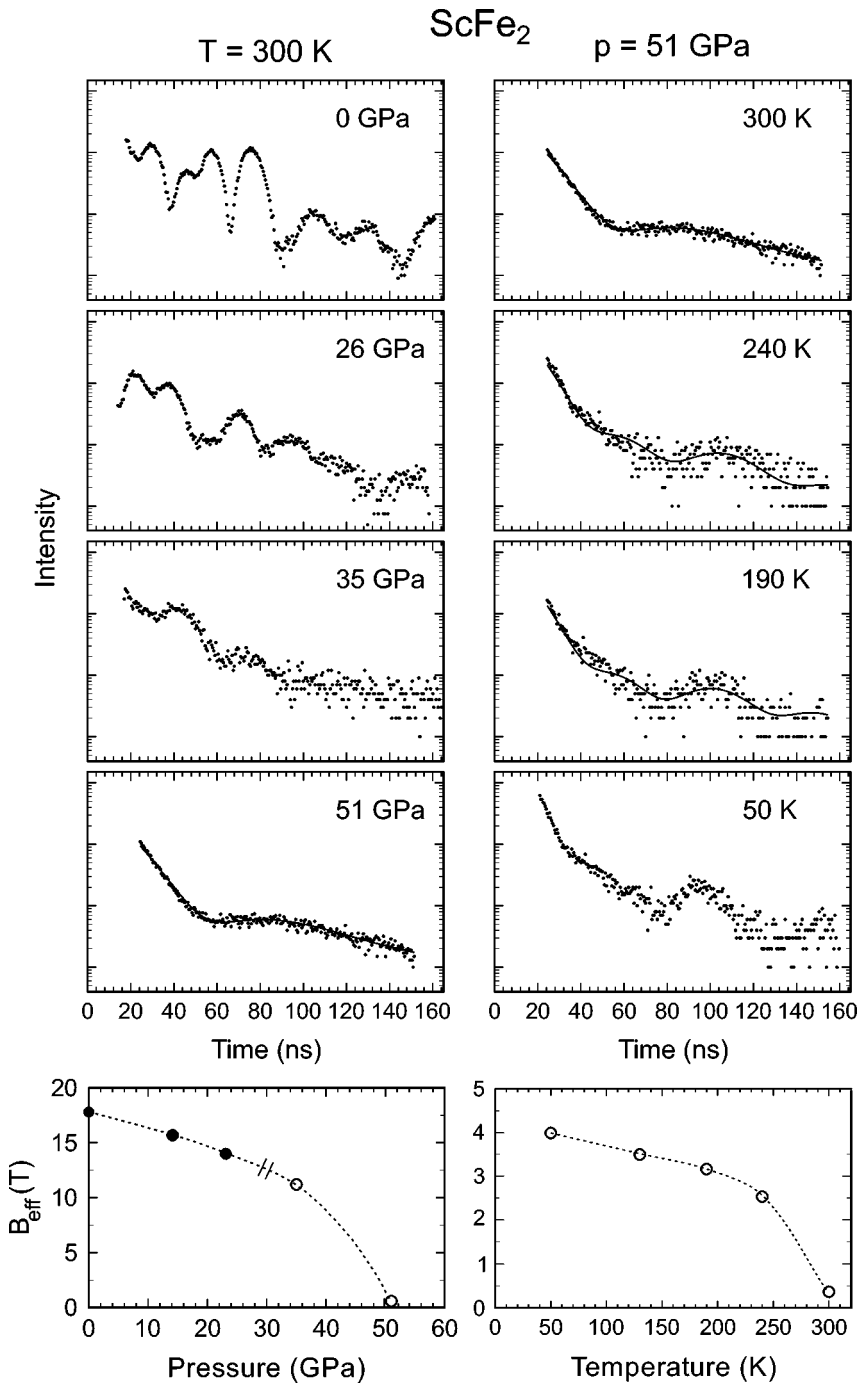

Figure 13. ^{57}Fe-NFS spectra of $ScFe_2$ at 300 K (left-hand panel) and for low temperatures at 51 GPa (right-hand panel). The extracted hyperfine fields are shown at the bottom, full symbols are for the fm phase, open symbols for the 6h sites of the afm phase.

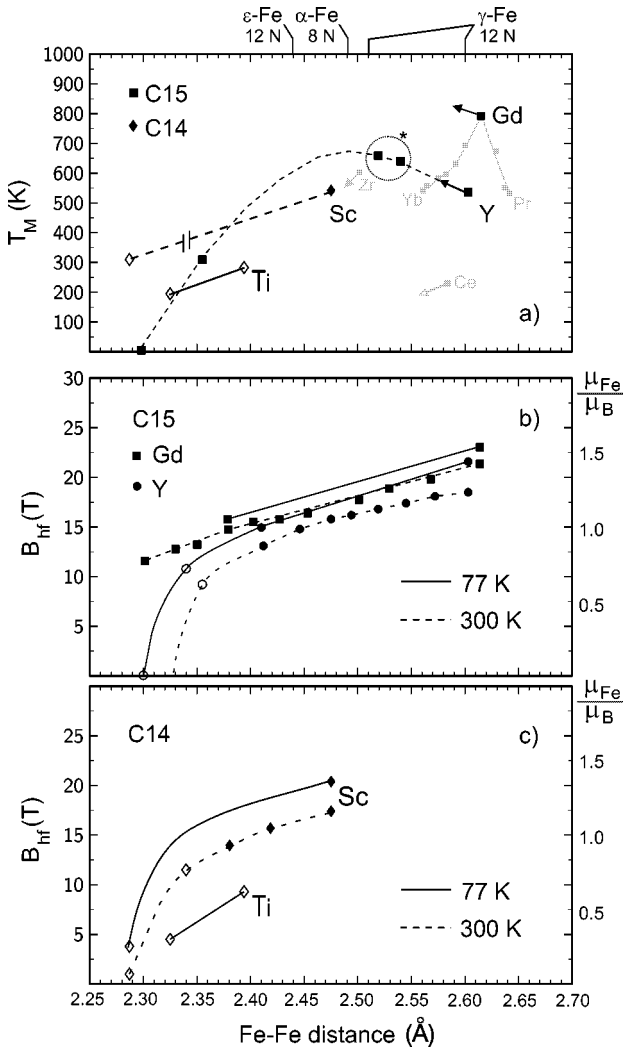

Figure 14. Magnetic ordering temperatures (a) and hyperfine fields (b) and (c) versus Fe–Fe distance for different RFe_2 Laves phase compounds. Full symbols are for fm ordering and open symbols for afm ordering. The arrows in (a) indicate the low-pressure behaviour of T_M, derived from resistivity studies [34]. The two T_C values for YFe_2 marked with * were obtained from XRD experiments measuring the magneto-volume anomaly [31]. The proportional behaviour of B_{hf} and the iron moment μ_{Fe}, marked on the left-hand axis of (b) and (c), is given in [26].

the Fe–Fe distances and coordination numbers N for the different phases of pure Fe with the data for γ-Fe mentioned above. Within the pressure range of the present study, we reduce the lattice parameter by more than 11%, which is two times more than the variation within the C14 and C15 RFe_2 series (caused by the different sizes of the R constituents), thereby probing explicitly the dependence of the Fe moment formation on the Fe–Fe distance. This information is contained in the variation of

the ^{57}Fe hyperfine fields, shown in figures 14(b), (c), which scale directly with the Fe moments [35].

Of particular interest is the variation of the magnetic ordering temperature in YFe_2, which increases from $T_C = 535$ K at ambient pressure to 650 K at 15 GPa [31] and then drops at higher pressures to 300 K around 75 GPa and vanishes around 105 GPa. This behaviour is indicated in figure 14(a), as a guide to the eyes, by a dashed line. The magnetic moments at the Fe sites, on the other hand, show a continuous decrease and then, at an Fe–Fe distance around 2.40 Å, a rapid drop and disappearance at 2.35 Å. Such a behaviour is discussed by Wohlfahrt [36] in a simple model of magnetic ordering in a band magnet and its pressure/volume dependence.

The Stoner criterion ($ID(E_F) > 1$) for the occurrence of ferromagnetic ordering in itinerant electron systems combines two conditions for this ordering: the strength of the exchange interaction, which is described by the Stoner parameter I, and a high density of states $D(E_F)$ at the Fermi energy. Although developed for ground state properties at $T = 0$ K, it can be extended to finite temperatures and provides a description of the two competing pressure effects on the ordering temperature T_C. First, pressure enhances the overlap of the atomic wave functions giving rise to an increase of the exchange interaction I. This leads to an increased stability of the magnetic phase, i.e., to a higher T_C. This behaviour is well known for systems with localized magnetic moments, e.g., pure 4f systems. However, in itinerant magnetism the band moment is affected by pressure. The 3d-bandwidth W increases with decreasing interatomic distance r ($W \propto r^{-5}$, see [36]) and consequently $D(E_F)$ is lowered. Both effects lead to a smaller 3d band moment, as observed by the decrease of the magnetic hyperfine fields with pressure (see figure 14(b), (c)).

From these arguments a simple formula was derived for the pressure derivative of T_C [36]:

$$\frac{dT_C}{dp} = \frac{5}{3}\kappa T_C - \frac{\alpha(p)}{T_C}, \tag{4.1}$$

where κ denotes the compressibility and $\alpha(p)$ a coefficient which increases with pressure. In the present case, the first term describes the increase of exchange interaction (which scales with T_C) and the second term the reduction of the band moment with decreasing Fe–Fe distance. As reflected by the YFe_2 data in figure 14(a) the first term is stronger at lower pressure, before the continuous reduction of the Fe 3d-moment becomes dominant and reverses the sign of dT_C/dp. In the pressure range 70–100 GPa, corresponding to an Fe–Fe distance of 2.40–2.35 Å, the Fe moment and concomitantly the magnetic order disappear. For a more detailed discussion additional data are needed in this pressure range.

We want to mention that the magnetic behaviour of YFe_2 as a function of lattice parameter is of great interest also for theoretical band structure calculations. At ambient pressure, the Fe moment and also an induced moment at the Y site are well described by such calculations [35]. We also want to point out that the C15 structure of YFe_2

(and $GdFe_2$) may change, according to the behaviour indicated in figure 14, to the C14 structure at pressures above 50 GPa.

A further interesting point is the change of the magnetic ordering type from fm to afm in the C14 systems, as observed for the first time in $ScFe_2$. Future experimental and theoretical work is needed to derive a complete magnetic phase diagram for the RFe_2 C14 systems.

5. ^{151}Eu-NFS studies of isomer shifts, valence transitions and magnetism

5.1. Introduction

^{151}Eu nuclear scattering of synchrotron radiation was only recently observed at ESRF (Grenoble) [37] and at TRISTAN (KEK, Tsukuba) [38] and also successfully applied for hyperfine spectroscopy [37]. The ^{151}Eu-resonance is known, due to the large change in the nuclear charge radii, for its extreme sensitivity for the measurements of isomer shifts of divalent and trivalent Eu systems [39]; this resonance is therefore the most suited and widely used from all rare-earth Mössbauer resonances to study temperature and/or pressure induced valence transitions or the phenomena of intermediate valence [40].

EuM_2Si_2 intermetallics (M = d-transition or noble metal) with tetragonal $ThCr_2Si_2$ structure are known for temperature- and pressure-induced valence transitions with $EuCu_2Si_2$ and $EuPd_2Si_2$ as most prominent examples [40], while isostructural EuM_2Ge_2 systems are stable divalent at ambient pressure [41,42]. After a short introduction in section 5.2 to the measurements of ^{151}Eu isomer shifts by the NFS-technique with Eu^{2+} and Eu^{3+} reference absorbers, we report in section 5.3 on an h.p. NFS study of the Eu valence transition in $EuNi_2Ge_2$.

In section 5.4 we present a study of the magnetic ordering in the CsCl-type h.p. phase of EuTe. Here conflicting results on the magnetic properties of the NaCl and CsCl phases of EuTe from a ^{151}Eu-Mössbauer study [43] and a recent neutron study [44] should be clarified by the present NFS-studies, where we reached higher pressures necessary to form the pure CsCl-phase of EuTe.

5.2. The measurement of isomer shifts

In normal Mössbauer spectroscopy the isomer shift of an absorber is measured with respect to the source, here mostly ^{151}Sm:SmF_3, with an isomer shift identical to that of EuF_3 used as a reference with "zero" isomer shift [39]. In NFS measurements, the isomer shift of an absorber is measured against a reference absorber. Here we used EuS and EuF_3 as reference systems for the relative isomer shift determination. The ^{151}Eu-NFS studies were performed at beamline ID18 of ESRF.

In figure 15 we show the ^{151}Eu-NFS spectra of these absorbers measured alone and sandwiched behind each other. When measured alone, the spectra are modified only by thickness effects, which are very pronounced in the EuF_3 spectrum. The

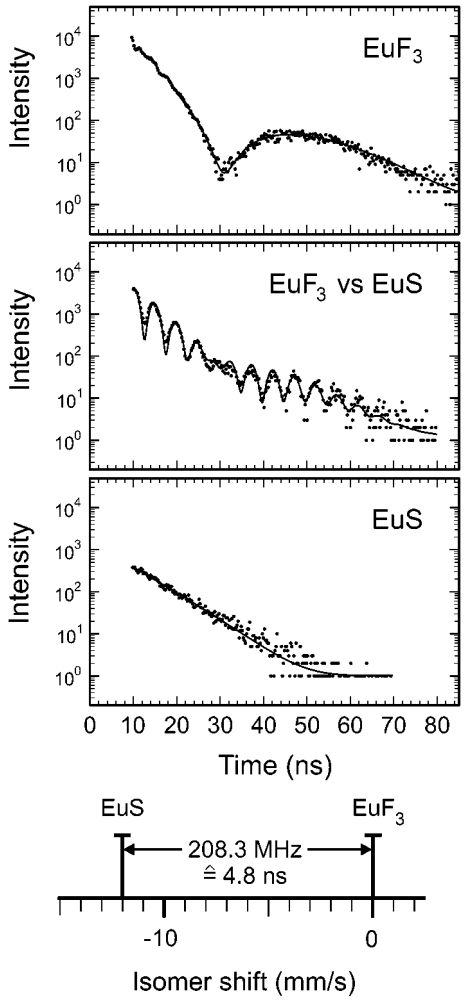

Figure 15. ^{151}Eu-NFS spectra of EuF_3, EuF_3 + EuS, and EuS. The pronounced minimum in the EuF_3 spectrum is due to thickness effects, the beating in the (EuF_3 + EuS) spectrum results from the difference in isomer shifts as depicted in the bar diagram at the bottom.

Bessel minimum at 30 ns indicates an effective thickness about twice as large as for the EuS spectrum. In the combined EuF_3+EuS spectrum, the strong beats with a period of 4.8 ns (208 MHz) correspond to a difference in isomer shift of 11.77(8) mm s^{-1}, in excellent agreement with the standard notation of (−)11.93(8) mm s^{-1} between EuS and EuF_3 [40]. The additional weak modulation of the beat amplitudes is due to thickness effects. As demonstrated in [37] for EuS/Eu_2O_3, the combined beat spectrum of EuS and EuF_3 can be used to derive the small quadrupole splitting in monoclinic EuF_3, which is not resolvable with normal ^{151}Eu-Mössbauer spectroscopy [45].

5.3. ^{151}*Eu-NFS of the pressure-induced valence transition in* $EuNi_2Ge_2$

The pressure experiments were performed at room temperature with an h.p. cell with boron carbide (B_4C) anvils allowing pressures up to 15 GPa with a sample diameter of 1 mm, using more than half of the monochromatized beam size. The sample was embedded in epoxy together with NaCl, which served as pressure marker. The pressure was determined before and after the NFS experiments by energy dispersive X-ray diffraction.

Figure 16 shows the h.p. NFS spectra of $EuNi_2Ge_2$, measured against EuF_3 (0–5.4 GPa) and EuS (5.4–10 GPa). The observed beats arise exclusively from the isomer shift differences between $EuNi_2Ge_2$ and the reference absorbers. The spectrum at ambient pressure versus EuF_3 exhibits, as in the case of the $EuS + EuF_3$ spectrum, the typical beats between a metallic Eu^{2+} system and the EuF_3 reference with an additional Bessel minimum at 30 ns. The beat frequency of 162 MHz corresponds to an isomer shift of $(-)9.40\ \mathrm{mm\,s^{-1}}$, in perfect agreement with standard ^{151}Eu-ME [42]. Around 4 to 5 GPa the more complex spectra indicate a distribution of mixed-valent states already shifted near to the trivalent state. For this reason, an additional spectrum was measured against the divalent EuS reference, now with a better resolution for the isomer shift. This illustrates the fact that, as with the other hyperfine interactions, large energy differences with repeated beat structures in the time spectra can be much better determined than small energy differences. At higher pressures the trivalent state is approached and the valence transition is completed at 10 GPa, as depicted in the diagrams in figure 16. This was also checked with the same h.p. cell after the NFS study with conventional ^{151}Eu-Mössbauer spectroscopy [45,46].

5.4. ^{151}*Eu-NFS study of magnetic ordering in the h.p. CsCl-phase of EuTe*

The EuX chalcogenides (X = O, S, Se, Te), crystallizing in the NaCl structure, are considered as model systems for Heisenberg magnetism because of the spin-only $J = S = 7/2$ 4f-moment of Eu^{2+}. They have been extensively studied with energy-resolved ^{151}Eu-ME under high pressure and also with high external fields [47–50]. The EuX series exhibit a pressure-induced structural phase transition from the NaCl phase to the CsCl phase at pressures ranging from 40 GPa for EuO to 11 GPa for EuTe with broad transition regions [51]. Here we report on a study of EuTe in both phases with the new ^{151}Eu-NFS technique [45] and compare the results with those from traditional ^{151}Eu-ME [43], performed in the coexistence range of the NaCl and CsCl-phase. The sample was pressurized in a diamond-anvil cell with 0.5 mm absorber diameter. The presence of the CsCl and NaCl phase at 15 GPa was confirmed by XRD measurements performed before the NFS studies as well as the complete transition to the CsCl phase at 20 GPa after the NFS studies [45].

EuTe orders antiferromagnetically at $T_N = 9.6$ K in the NaCl-phase at ambient pressure; a magnetically modulated NFS spectrum of this phase taken at 4.2 K is shown in figure 17 (right-hand panel at the bottom), which was fitted with a hyperfine field of 23.3(5) T, in excellent agreement with [47,49]. From conventional ^{151}Eu-Mössbauer

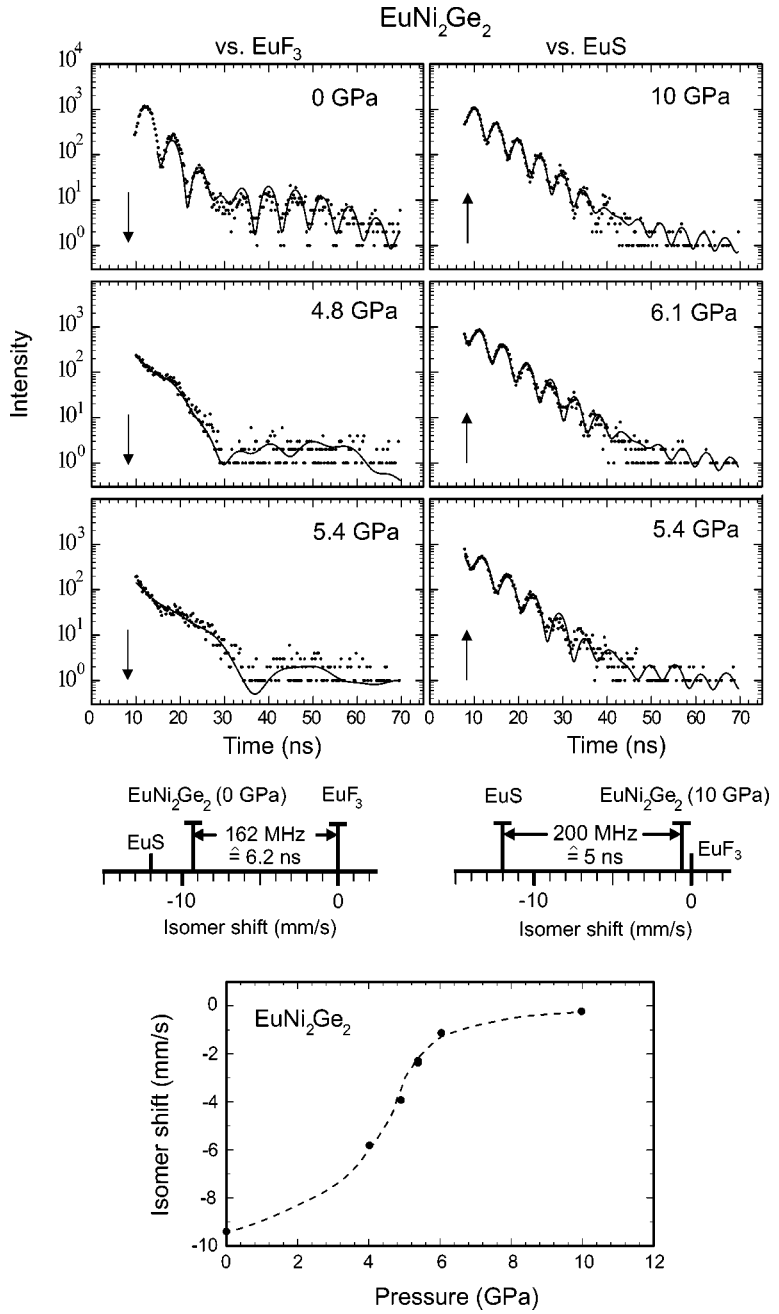

Figure 16. ^{151}Eu-NFS spectra of $EuNi_2Ge_2$ at various pressures measured against EuF_3 (left-hand panel) and EuS (right-hand panel). The isomer shift differences between $EuNi_2Ge_2$ and the reference absorbers are depicted in the bar diagram. The valence transition is shown in the isomer shifts vs. pressure diagram at the bottom [45,46].

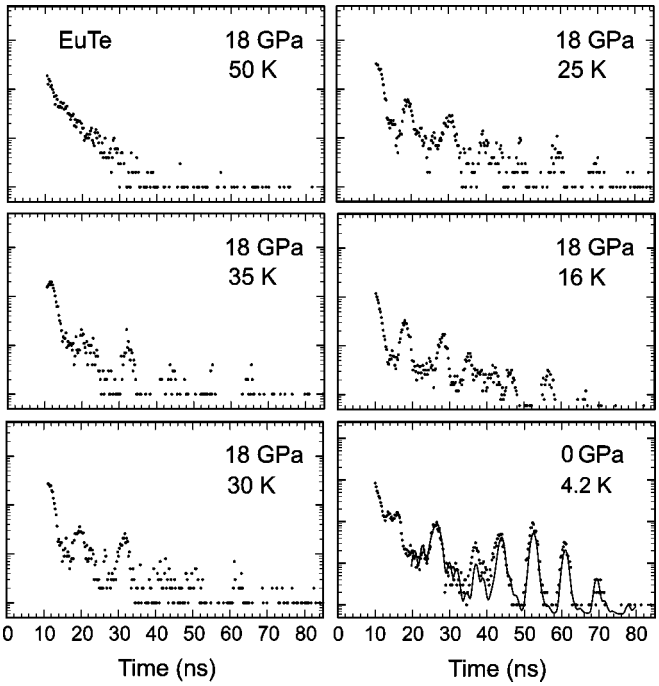

Figure 17. ^{151}Eu-NFS spectra of EuTe in the CsCl-phase at 18 GPa and various temperatures. The NFS spectrum of EuTe in the NaCl-phase at 0 GPa and 4.2 K is shown in the right-hand panel at the bottom.

studies of EuTe up to 13 GPa [43], ferromagnetic order was derived for the NaCl phase from the observed (larger) saturation hyperfine fields at pressures above 9 GPa, similar to the case of ferromagnetic NaCl-type EuTe in an external magnetic field [49]. In addition, the ordering temperature of the NaCl-phase was found to increase strongly with pressure.

Figure 17 shows NFS spectra of EuTe in the (almost pure) CsCl-phase at 18 GPa and various temperatures. At 50 K, one observes in the NFS spectrum only the nearly exponential decay without any hyperfine interactions, whereas at lower temperatures the magnetic beat structures reveal a magnetically ordered state. From a preliminary evaluation of $B_{\mathrm{hf}}(T)$ we determine the magnetic ordering temperature as $T_{\mathrm{C}} = 42(5)$ K at 18(1) GPa. This is a dramatic increase for the CsCl-phase in comparison to 16 K observed at 10 GPa for the NaCl-phase (see figure 18). It resembles the strong increase of T_{C} in NaCl-type EuO [50], EuS and EuSe [48] with the reduction of the lattice parameter, caused by the 4f–5d–4f exchange of the direct Eu–Eu overlap. This behaviour can be qualitatively explained by the fact that the Eu–Eu distance of the six nearest Eu neighbours in CsCl-type EuTe, 3.650 Å at 20 GPa [46], is nearly the same as in NaCl-type EuO (3.637 Å) with twelve nearest Eu neighbours and $T_{\mathrm{C}} = 69$ K.

The present h.p. NFS results on EuTe (12 spectra) were obtained within about 12 h. For comparison, one spectrum of EuTe measured in the same cell at 20 GPa with standard ^{151}Eu-Mössbauer spectroscopy needs 20 days. As in the case of the

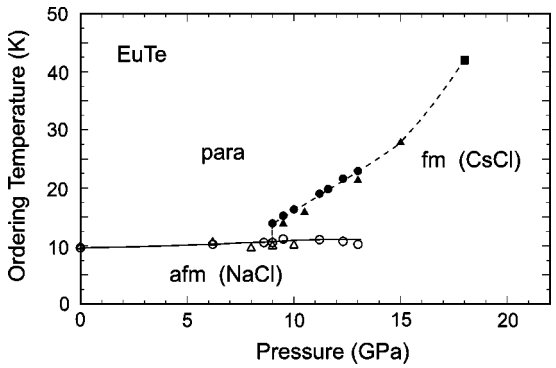

Figure 18. Magnetic ordering temperatures of EuTe as a function of pressure. Data for the NaCl phase are from ME (circles) [43] and neutron diffraction (triangles) [44]. The value for the CsCl phase (square) is from the NFS study [45,46].

^{57}Fe-resonance, this again demonstrates the superiority of the NFS method for h.p. studies of magnetism. Future ^{151}Eu-NFS studies will benefit from a cryostat allowing the application of large polarizing fields on the h.p. cell in a wide temperature range. This enables an easy discrimination between antiferromagnetic or ferromagnetic order in the NFS spectra [37,49]. The present NFS studies also demonstrate the elegance for measuring precise ^{151}Eu isomer shifts as well as the extreme feasibility of this method for h.p. studies of isomer shifts and valence transitions.

6. Conclusions and outlook

6.1. Comparison of h.p. NFS studies with normal h.p. ME studies

The presented NFS measurements of YFe_2 and $GdFe_2$ are, to the best of our knowledge, the first NFS studies above the "Mbar-borderline". Conventional ^{57}Fe-Mössbauer studies crossed this line in a recent investigation of $Fe_{0.94}O$ [12]. We want to mention that all of the presented h.p. NFS studies were accompanied by normal ME studies of the same sample in the same h.p. cell, performed before or after the NFS studies [30,45]. These ME measurements, also performed at lower temperatures, took weeks instead of hours. They delivered similar information on hyperfine fields and quadrupole interactions as well as on the isomer shifts; this important hyperfine parameter revealed in the case of YFe_2 a huge change of $-0.65\ \mathrm{mm\,s^{-1}}$ between 0 and 105 GPa [30]. Of course, isomer shifts can also be measured with the NFS method, as demonstrated in section 5.2 for the ^{151}Eu-resonance. Finally, the NFS data on the $\alpha \rightarrow \varepsilon$ transition in Fe revealed the sensitivity of the method to the spatial distribution of domain structures in the sample, an aspect which energy-resolved Mössbauer spectroscopy cannot provide.

In the case of complex or multisite magnetic-dipole/electric-quadrupole interactions, the extraction of the pressure dependence of the hyperfine parameters from the

NFS spectra demands accompanying ME studies of the investigated sample. The same holds for pressure-induced structural phase transitions. In this case, additional XRD studies are mandatory, if possible on the same sample in the same h.p. cell. Considering these conditions, the unique quality of the NFS method for fast determination of magnetic properties and ordering temperatures at very high pressure can be fully exploited. Similar applications of NFS experiments on the electric properties of geophysical specimens up to 68 GPa are reported in [52]. NFS has recently also been applied using the ^{119}Sn-(23.8 keV) resonance [53] to study strongly correlated electron systems under h.p. [54].

6.2. Inelastic nuclear scattering (INS) under high pressure

Future developments of nuclear scattering experiments under pressure will be applied for the new technique of inelastic scattering [17,18], making the study of local phonon density-of-states under h.p. possible. For this purpose, the detection of fluorescence photons, in the case of ^{57}Fe with 6.4 and 7.1 keV in the 4π direction, is very difficult, because the transmission through conventional gasket materials like $Ta_{90}W_{10}$ or inconel is very low. Therefore low-Z materials like epoxy or beryllium for the gasket have to be used. With such gasket materials we carried out first ^{57}Fe-INS studies on metallic iron at 10 GPa (still in the α-phase) and 24 GPa (pure ε-phase) [55]. Similar preliminary studies with the ^{119}Sn (23.8 keV) resonance on β-tin and γ-tin were performed up to 20 GPa at the Advanced Photon Source (APS, Argonne National Laboratory, Chicago) [56].

6.3. Focusing optics

In section 1 we already mentioned two important features of NFS experiments for h.p. studies: the high brilliance of synchrotron radiation and the nearly perfect suppression of non-resonant background in the time mode detection. Up to now, only few experiments were carried out with focusing elements in the beamline optics. The intensity loss due to the mismatch between beam size and sample size is shown in figure 19 for NFS and conventional ME experiments. For NFS studies at 100 GPa a typical sample diameter is 80 μm and only 0.5% of the unfocused incoming beam (1 mm^2) is utilized. This loss factor of 200 at 100 GPa can be substantially reduced when focusing optical elements are used to concentrate the flux of synchrotron radiation on the pressurized sample. The gain depends on the reduced beam size and the efficiency of the focusing element, here bent crystals [57], Fresnel zone plates [58] or the compound refractive lenses (CRL) developed by Snigirev et al. [59]. Such lenses have recently been installed in the beamline optics of ID18 at ESRF and may provide spot sizes below 100 μm. The small acceptance of this lens does not allow the use of all incoming intensity. In figure 19, we present an estimation of the effectiveness for such a focusing element with 10% acceptance and a spot size of 100 μm in diameter. At a sample size of 100 μm (or pressures around 100 GPa), the flux through the sample increases by a factor 10–20, which will reduce measuring times from 1–2 h to 10 min.

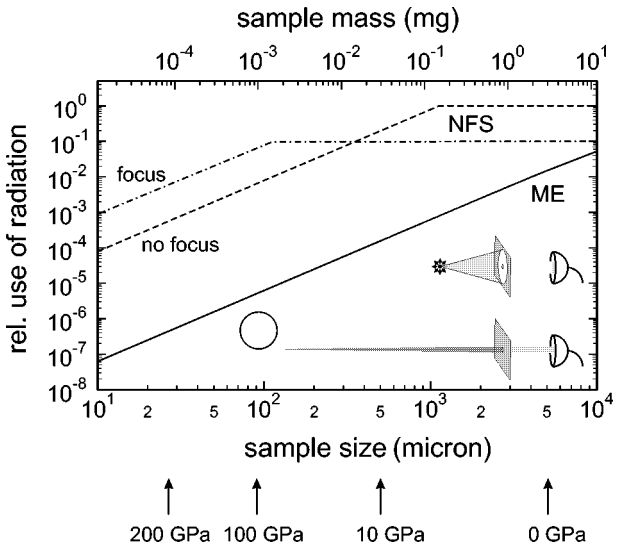

Figure 19. Relative use of source radiation for NFS (with and without focusing optics) and ME. For the focusing optics in this example an efficiency of 10% and a spot size of 100 μm is assumed. The sample mass is calculated for a sample thickness of 30 μm and a density of 5 mg/cm^3.

This increase leads to a new quality for NFS h.p. experiments; even pressures as large as 300 GPa, probing the inner parts of the earth, seem possible in the near future.

Acknowledgements

The work was supported by the German Ministry for Research and Technology (BMBF, Verbund 43). We want to thank Alfred Baron, Aleksandr Chumakov, Hanne Grünsteudel, Olaf Leupold, Joachim Metge and Rudolf Rüffer for their friendly co-operation in many stages of the h.p. studies at ESRF. We acknowledge the help of Hans-Josef Hesse, Gerd Reiß and Markus Winzenick with the XRD measurements. The Paderborn group benefitted from the h.p. ME studies performed by Jiangang Lu and Matthias Strecker in their Ph.D. theses as well as by Marianne Pleines and Kirsten Rupprecht in their Diploma theses. The whole Paderborn group thanks the mechanical workshop headed by Franz Risse. HG is particularly grateful to Dean Taylor (Los Alamos, USA) and Jean Thomasson (CEA Grenoble, France) for an introduction to their h.p. techniques.

References

[1] S.L. Ruby, J. Phys. C 6 (1974) 209.
[2] E. Gerdau et al., Phys. Rev. Lett. 54 (1985) 835.
[3] J.B. Hastings et al., Phys. Rev. Lett. 66 (1991) 770;
U. van Bürck et al., Phys. Rev. B46 (1992) 6207;

E. Gerdau and U. van Bürck, in: *Resonant Anomalous X-Ray Scattering, Theory and Applications* (Elsevier, Amsterdam, 1994) p. 589.
[4] G. Faigel et al., Phys. Rev. Lett. 58 (1987) 2699;
T. Ishikawa et al., Rev. Sci. Instrum. 63 (1992) 1015;
T. Toellner et al., Proc. SPIE 1740 (1992) 218.
[5] S. Kishimoto, Nucl. Instrum. Methods A 309 (1991) 603;
A.Q.R. Baron et al., Nucl. Instrum. Methods A 343 (1994) 517 and ibid. 352 (1995) 665.
[6] R.V. Pound and G.A. Rebka, Phys. Rev. Lett. 4 (1961) 337.
[7] S. Nasu, Hyp. Interact. 90 (1994) 54.
[8] R. Rüffer and A.I. Chumakov, Hyp. Interact. 97/98 (1996) 589;
R. Rüffer et al., ESRF Newsletter 22 (1994) 12, and ESRF Highlights 1994/95, p. 36.
[9] W. Sturhahn and E. Gerdau, Phys. Rev. B 49 (14) (1994) 9285.
[10] A.Q.R. Baron et al., Phys. Rev. Lett. 77 (1996) 4808; see also this issue, section IV-3.1.
[11] G. Cort, R.D. Taylor and J.O. Willis, J. Appl. Phys. 53 (1982) 2064 and 8199.
[12] M.P. Pasternak et al., Phys. Rev. Lett. 79 (1997) 5046.
[13] D.L. Williamson, in: *Mössbauer Isomer Shifts* (North-Holland, Amsterdam, 1978) p. 317.
[14] M.P. Pasternak and R.D. Taylor, in: *Mössbauer Spectroscopy Applied to Magnetism and Materials Science*, Vol. 2 (Plenum Press, New York, 1996) p. 167.
[15] R.A. Forman, G.J. Piermarini, J.D. Barnett and S. Block, Science 176 (1972) 284.
[16] R. Lübbers, Diplom thesis, Paderborn (1994), unpublished.
[17] M. Seto et al., Phys. Rev. Lett. 74 (1995) 3828;
W. Sturhahn et al., Phys. Rev. Lett. 74 (1995) 3832;
A.I. Chumakov et al., Europhys. Lett. 30 (1995) 427.
[18] A.I. Chumakov et al., Phys. Rev. B 54 (1996) 9596.
[19] D. Bancroft, E.L. Peterson and S. Minshall, J. Appl. Phys. 27 (1956) 291.
[20] D.N. Pipkorn et al., Phys. Rev. A 135(6) (1964) 1604.
[21] D.L. Williamson, S. Bukshpan and R. Ingalls, Phys. Rev. B 6(11) (1972) 6126.
[22] R.D. Taylor, M.P. Pasternak and R. Jeanloz, J. Appl. Phys. 69(8) (1991) 6126.
[23] N. von Bargen and R. Boehler, High Pressure Res. 6 (1990) 133.
[24] H.F. Grünsteudel et al., Hyp. Interact. C 1 (1996) 509.
[25] H.F. Grünsteudel et al., Austral. J. Phys. 51 (1998) 453.
[26] E. Burzo, A. Chelkowski and H. Kirchmayr, in: *Landolt–Börnstein New Series III*, Vol. 19d2 (Springer, Berlin, 1990).
[27] K. Mori et al., J. Alloys Compounds 270 (1998) 35.
[28] Y. Nishihara and Y. Yamaguchi, J. Phys. Soc. Japan 54 (1985) 1122 and ibid 55 (1986) 920.
[29] J. Lu, Dissertation, Universität Paderborn (1999).
[30] J. Lu et al., in: *Conf. Proc.*, Vol. 50 (SIF, Bologna, 1996) p. 243.
[31] G. Reiß et al., unpublished results;
G. Reiß, Dissertation, Paderborn (1999).
[32] M. Strecker and G. Wortmann, Hyp. Interact. 120/121 (1999) 187.
[33] D.J. Keavey et al., Phys. Rev. Lett. 74 (1995) 4531 and references therein.
[34] M. Brouha and K.H.J. Buschow, J. Appl. Phys. 44 (1973) 1813.
[35] J.M.G. Armitage et al., J. Phys. F., Metal. Phys. 16 (1986) L141.
[36] E.P. Wohlfahrt, in: *Physics of Solids under High Pressure* (North-Holland, Amsterdam, 1981) p. 175.
[37] O. Leupold et al., Europhys. Lett. 35 (1996) 671; see also this issue, section IV-2.7.
[38] I. Koyama et al., Japan J. Appl. Phys. 35 (1996) 6297.
[39] E.R. Bauminger, G.M. Kalvius and I. Nowik, in: *Mössbauer Isomer Shifts* (North-Holland, Amsterdam, 1978) p. 661.
[40] I. Nowik, Hyp. Interact. 13 (1983) 89.
[41] G. Wortmann et al., Phys. Rev. B 43 (1991) 5261.

[42] H.-J. Hesse et al., J. Alloys Compounds 246 (1997) 220.
[43] J. Moser, G. Wortmann and G.M. Kalvius, unpublished results.
[44] I.N. Goncharenko and I. Mirebeau, Europhys. Lett. 37 (1997) 633, and Phys. Rev. Lett. 80 (1998) 1082.
[45] M. Pleines, Diplom thesis, University of Paderborn (1998), unpublished.
[46] M. Pleines et al., Hyp. Interact. 120/121 (1999) 181.
[47] U.F. Klein et al., J. Magn. Magn. Mater. 3 (1976) 50.
[48] J. Moser et al., J. Magn. Magn. Mater. 12 (1979) 77.
[49] Ch. Sauer, A.M. Zaker and W. Zinn, J. Magn. Magn. Mater. 38 (1983) 225.
[50] M.M. Abd-Elmeguid and R.D. Taylor, Phys. Rev. B 42 (1990) 11048.
[51] A. Jayaraman et al., Phys. Rev. B 9 (1974) 2513.
[52] L. Zhang et al., American Mineralogist 84 (1999) 447.
[53] S. Kikuta, Hyp. Interact. 90 (1994) 335;
E.E. Alp et al., Phys. Rev. Lett. 70 (1993) 3351;
A.I. Chumakov et al., Phys. Rev. B 58 (1998) 254.
[54] A. Barla et al., to be published.
[55] R. Lübbers et al., ESRF Report on experiment HS-583 (1998), and to be published.
[56] R. Lübbers et al., to be published.
[57] A.K. Freund et al., Proc. SPIE 3448 (1998) 1 and references therein.
[58] Di Fabrizio et al., J. Vac. Sci. Tech. B 11 (1998) 3855 and references therein.
[59] A. Snigirev et al., Nature 384 (1996) 49.